The Energetics of the Rapid Intensification of Hurricane Earl (2010)

Daniel Nielsen

A scholarly paper in partial fulfillment of the requirements for the degree of

Master of Science

August 2016

Department of Atmospheric and Oceanic Science, University of Maryland
College Park, Maryland

Advisor: Dr. Da-Lin Zhang

Table of Contents

Abstract

Tropical cyclone (TC) intensity changes are becoming better understood through research, although the Rapid Intensification (RI) stage is still difficult to predict. In this study, the energetics of Hurricane Earl (2010) were analyzed in order to provide a better understanding of how TCs generate and dissipate energy throughout their intensity and structural changes, including RI, the Secondary Eyewall Formation (SEF), and post-RI slow intensification and subsequent weakening. First, model simulations were verified against observations until a sound simulation was obtained, such that the model run accurately reflected observations in terms of track, intensity, and structure, including that of the SEF. Energy equations were then derived, and, using the model output in combination with these equations, calculations were performed in order to understand the evolution of the energy generation, dissipation, and other budget terms throughout the duration of the 120-h simulation. It was found that generation is the dominant budget term, and that it increases throughout RI, while the budget residual is small in areas outside of the boundary layer and upper-level outflow regions. The difference between positive and negative generation grows throughout RI, serving as a potential indicator of such intensification. Additionally, the evolution of bulk kinetic energy (BKE) was found to closely match the intensity changes of Earl. These results, although obtained from an analysis of Earl, can be widely applied to many rapidly intensifying TCs.

Acknowledgements

I would like to thank my graduate advisor, Dr. Da-Lin Zhang, for his continued support and guidance throughout my time in graduate school, as well as his enthusiasm for scientific research. Without his assistance, this work would not have been possible. I would also like to thank Dr. Jung Hoon Shin for all of his time spent running model simulations and helping me learn the various computing resources used to process, analyze, and visualize model and observational data. Finally, I would like to extend a special thanks to all of my instructors and advisors from both my undergraduate and graduate schools for their mentorship, and to my family and friends for their encouragement and support.

List of Tables

List of Figures

List of Symbols

ρ - air density

v – horizontal velocity

f – Coriolis parameter

F – frictional force

P – pressure

KE – kinetic energy

BKE – bulk kinetic energy

t - time

Chapter 1. Introduction

1.1 Tropical Cyclone Intensity Forecasting

Over the past few decades, major advances have made in forecasting tropical cyclone (TC) location. However, much less progress has been made in forecasting TC intensity (Rogers et al. 2006; DeMaria et al. 2005). This is likely attributable to the complexity of TC intensity changes, which involve multi-scale interactions between the storm and various aspects of the environment, such as vertical wind shear (VWS) and sea surface temperature (SST). As a result, errors in forecasting these variables lead to further problems with TC intensity forecasts. This is especially true for storms undergoing Rapid Intensification (RI), which is defined as an increase of about 15 m s^{-1} in the maximum sustained surface wind speed in a 24-h period (Kaplan and DeMaria 2003). One example of a storm that underwent RI is Hurricane Earl (2010), which rapidly intensified despite the presence of moderate VWS.

Previous studies of Earl have focused on various aspects of lower- and upper-level processes and their relation to RI. Chen and Gopalakrishnan (2015) determined, through the use of the Hurricane Weather Research and Forecasting (HWRF) Model, that the initially tilted vortex became aligned vertically during the late RI stage as a result of convective-scale subsidence and shear-induced mesoscale subsidence. Stevenson et al. (2014) showed that an inner-core lightning burst preceded RI, with most of it occurring within the Radius of Maximum Wind (RMW). Rogers et al. (2015) determined that convective bursts (CBs), mostly within the RMW, played a role in aligning the upper-level circulation center above the lower-level center. Additionally, Susca-Lopata et al. (2015) further investigated the relationship between CBs, the RMW, and RI, as well as

vortex alignment, finding that precipitation became more symmetric, and the vortex more aligned, following the rotation of deep convection from the downshear to the upshear region. Although these studies offer a breadth of information regarding RI and its relationship with other processes, they do not discuss the influence of storm energetics or the Eyewall Replacement Cycle (ERC) on RI and intensity changes of storms.

1.2 Kinetic Energy in Tropical Cyclones

It is known that TCs concentrate large amounts of energy, particularly kinetic energy (KE), within the inner-core region. However, uncertainty exists with regards to the specific relationship between energy generation and dissipation, especially during RI. Flow results in generation or dissipation depending on whether the cross-isobaric component is directed toward low or high pressure. In this study, however, all energy changes due to cross-isobaric flow, whether positive or negative changes, will be referred to as positive or negative generation. Dissipation, on the other hand, will refer to dissipation due to friction, viscosity, and other diffusional effects. In order to better assess and predict TC strength and intensity change, a thorough understanding of the KE budget is required.

Several observational and modeling studies have been performed to better understand the KE production within TCs. Frank (1977) used rawinsonde composite data to calculate the KE and moist static energy budgets of TCs, showing how TCs import KE from their environments and produce most KE in the near-surface layer. McBride (1981) used data from the Atlantic and Pacific basins to calculate energy budgets for tropical cloud clusters. It was later found that intensifying storms are characterized by a synoptic-scale increase in KE and a decrease in latent energy (LE), which is consumed during

latent heat release. Such observational studies, while practical in methodology, are limited by the poor resolution of observations, and caution must be taken in interpreting their results. The lack of observational data over the tropical oceans is troublesome for studying important energetic processes that occur in the inner-core convective regions, because the study of these processes requires high resolution data, which is extremely difficult to obtain through in situ measurements, especially in the tropical ocean regions.

For these reasons, mesoscale models have become increasingly important tools in studying the intensity, evolution, and structure of TCs because of their ability to provide dense and high-quality data. Several studies have investigated the energetics as well as the structures of TCs through the use of high-resolution modeling. For instance, Tuleya and Kurihara (1975) used the Geophysical Fluid Dynamics Laboratory (GFDL) TC model to simulate an idealized TC and used to it to calculate budgets of KE and LE at different stages of the storm development. They found that the mean flow is the primary contributor to the KE changes, although the contribution from eddies is not fully negligible. Hogsett and Zhang (2009) performed calculations on energy conversions, especially between KE and LE, associated with Hurricane Bonnie (1998). Additionally, other studies have used cloud-resolving models to simulate the structure and evolution of hurricanes (Braun 2002; Zhu et al. 2004). As a result, TC researchers have been able to confidently investigate inner-core dynamics and thermodynamics of storms through modeling during recent years.

1.3 **Objectives of this Study**

The main focuses of this study are to validate the model simulation against observations and to analyze the energetic changes that occur before, during, and immediately following

RI. Additionally, structural changes of Earl will be examined, including those associated with the Secondary Eyewall Formation (SEF), also referred to as the ERC. These goals will be accomplished by investigating the following:

- Performance of the model simulation relative to observations, regarding track, intensity, and structure
- Intensity and structural changes of Earl, especially during the RI period, which occurred despite the presence of moderate VWS
- Kinetic energy budget, including generation and dissipation, in relation to RI
- SEF of Earl and its relation to energetic and intensity changes

Chapter 2. Model Description and Methodology

2.1 Model Description

In order to study the energetics of Hurricane Earl, Version 3.4.1 of the Weather Research and Forecasting (WRF) model is used to simulate the storm, so that its movement, intensity, and evolution can be analyzed. The model contains a four-way nested domain (27/9/3/1 km), with the inner two domains being storm-following grids with the storm located at the center of these domains. Additionally, the horizontal grid dimensions vary among the four domains, which are more specifically defined in Table 1. The model domain coverage can be seen in Figure 1. The outer three domains are initialized at 1800 UTC 26 August, while the innermost simulation begins at 1200 UTC 27 August. All simulations end at 1200 UTC 01 September. Model initial and boundary conditions are obtained from 1°× 1° resolution National Centers for Environmental Prediction (NCEP) final analysis, and SST is also retrieved from the NCEP analysis at the model initial time and set constant during the entire simulation period.

The Kain-Fritsch cumulus parameterization scheme (Kain 2004) is used within the two outer domains, while convection is explicitly simulated in the two inner domains. On the other hand, the Thompson microphysics scheme, along with the Yonsei University planetary boundary layer (PBL) parameterization (Hong et al. 2005) and the improved surface flux scheme for hurricane force winds (Donelan et al. 2004; Davis et al. 2008), are applied to all domains.

Grid Resolution	27/9/3/1 km (3 and 1 km domains are storm-following nests) 27/9/3 km domains are initialized at 1800 UTC/26 August 1 km domain is initialized at 1200 UTC/27 August
Cumulus Parameterization	Kain-Fritsch scheme is used in 27/9 km domains No cumulus scheme in 3/1 km domains
Planetary Boundary Layer	Yonsei University (YSU) scheme
Microphysics	Thompson scheme
Vertical Levels	50 vertical levels with a 30-hPa top

Table 1: Model configuration

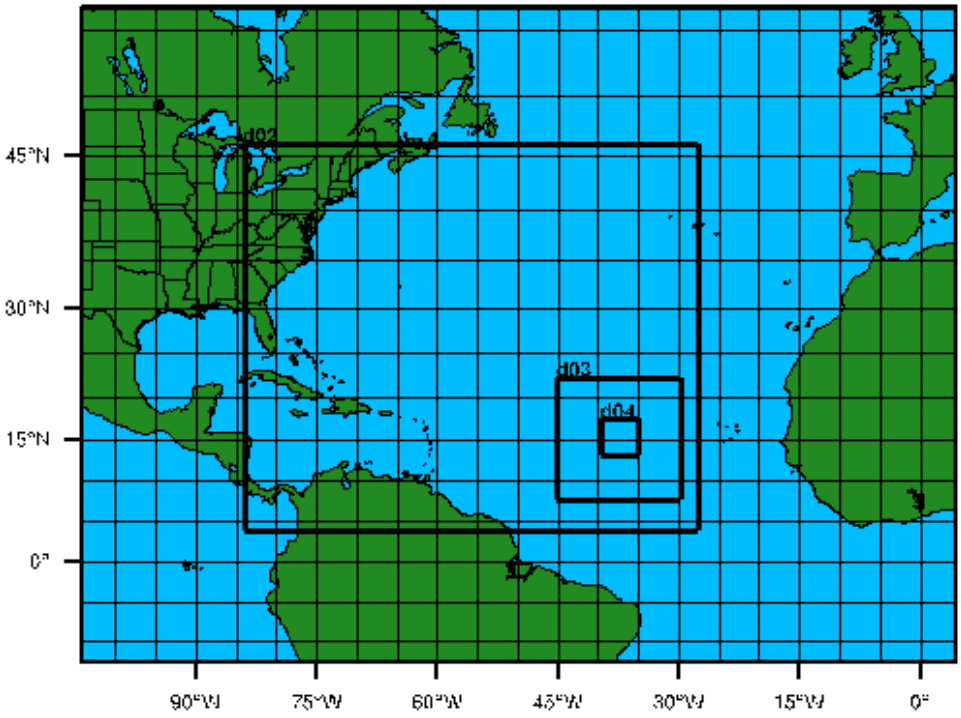

Figure 1: Model domain; domains 3 (d03) and 4 (d04) are storm-following nests

2.2 Model Verification

2.2.1 Track and Intensity

Earl developed into a tropical storm on 25 August before undergoing RI beginning at 0600 UTC 29 and reaching its first intensity peak around 0600 UTC 31. During RI, the maximum wind increased from 28.3 m s^{-1} to 59.1 m s^{-1} with a minimum central pressure of 931 hPa at its peak. After reaching its peak intensity just north of Puerto Rico, Earl began to weaken around 31 August as the storm started moving northwestward (Figure 2). The central pressure increased to 942 hPa and the maximum wind weakened to 54 m s^{-1} at 0600 UTC 1 September. Although intensity changes continued after this point, our simulation ends at 1200 UTC 01 September as we are mainly interested in the RI stage.

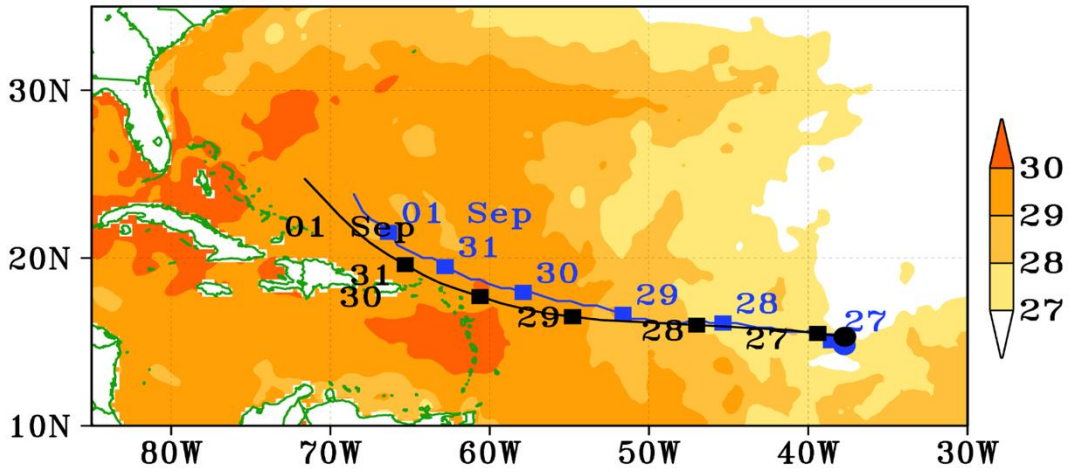

Figure 2: Comparison of the simulated storm track (blue) and best-track/observations (black) superimposed with the model sea-surface temperature (shaded, °C), which is obtained for the model initial time

Figure 3 shows the simulated and observed storm intensities in terms of both minimum central pressure and maximum wind. Due to the presence of a strong TC vortex structure in the NCEP analysis, the initial intensity of the simulated storm is about 10 hPa weaker than the best track. The model, however, captures the intensity changes of the storm fairly

accurately, especially during the RI period. The simulated storm begins RI around 0600 UTC 28 August, approximately 24 hours prior to that of the observed storm. However, the simulated storm completes RI around 0000 UTC 30 August, about 12 hours before that of observed Earl, although the simulated system continues to intensify at a slower rate until 01 September. Despite these minor inaccuracies, the general intensification pattern is similar between the two, although the model over intensifies the storm during RI, but only by about 15 hPa, which equates to an error of 10-15%. After RI, the simulated Earl begins to weaken moderately, while the observed storm weakens very slightly.

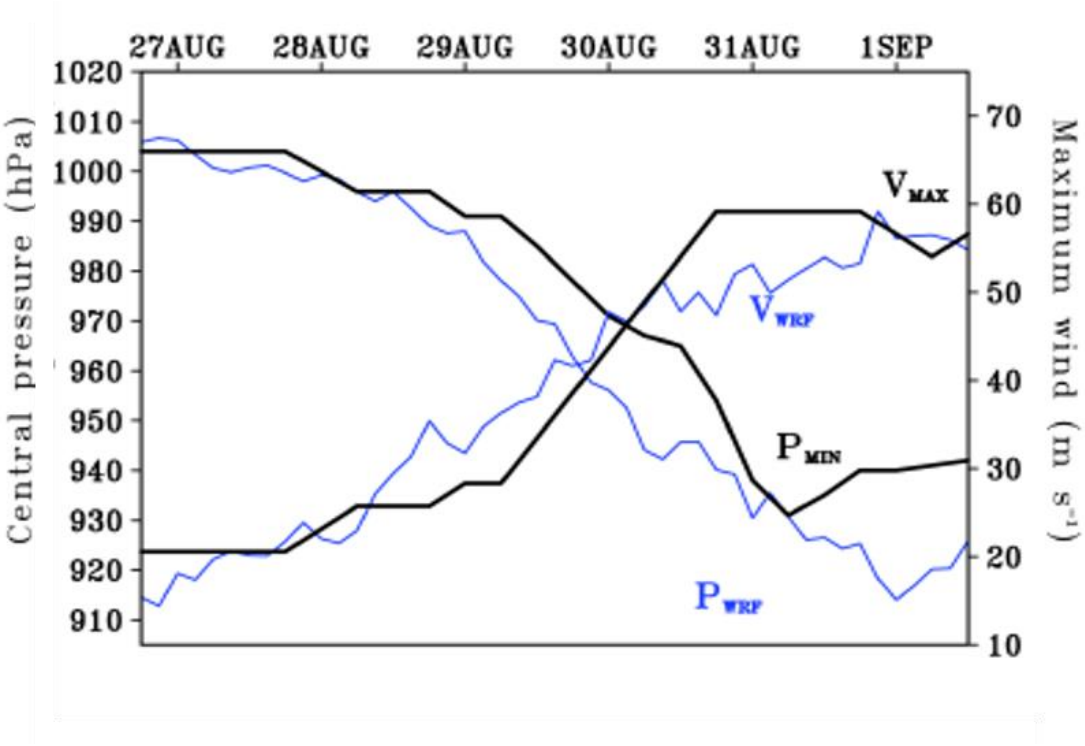

Figure 3: Comparison of the simulated minimum central pressure (P_{WRF}) and 10 m maximum wind (V_{WRF}) to the NHC best track (P_{MIN}, V_{MAX}); model data is from the 27 km domain

2.2.2 Structure

Earl underwent an SEF beginning on 30 August and continuing until 01 September. As part of this cycle, a secondary eyewall formed outside of the inner eyewall, cutting off

moisture and heat fluxes to the center of the storm, eventually resulting in the collapse of the inner eyewall and the end of the storm's RI. The model simulation accurately captures the structure of the storm with regards to the SEF. However, it is 12-18 hours late in doing so, which can be seen in Figure 4. For instance, while the observed Earl displayed a collapsing inner eyewall by 2300 UTC 31 August, the simulated Earl still shows a concentric double eyewall at that time. It is not until 01 September that the collapse of the inner eyewall begins. This is likely associated with the model's tardiness regarding the end of the intensification period, as the SEF essentially acts to end RI (or slightly slower intensification). The SEF associated with simulated Earl is analyzed in more detail in Section 3.1.

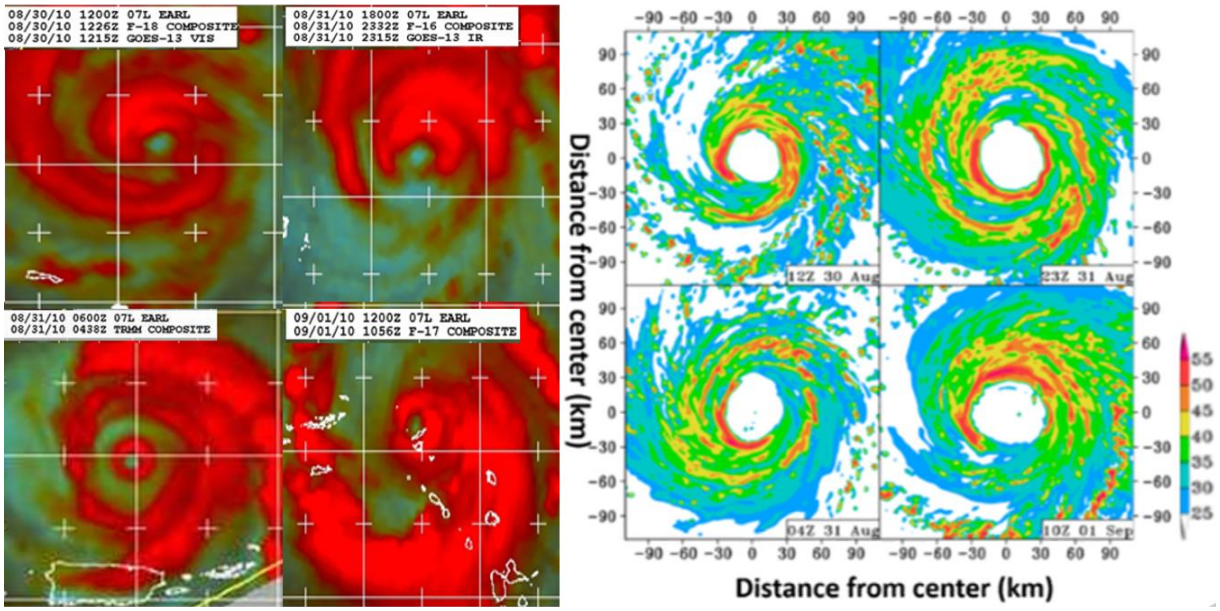

Figure 4: (Left) Microwave satellite imagery of Earl (from the Naval Research Laboratory's tropical cyclone webpage) and (right) 1.5 km simulated radar reflectivity (shaded, dBZ) at the times indicated; obtained from innermost domain

2.3 Kinetic Energy Equations and Methodology

In order to study the kinetic energy changes associated with the storm over the course of the simulation, budget equations are derived from basic equations following the methodology of Hogsett and Zhang (2009). Kinetic energy per unit volume is defined as

$$KE = \frac{\rho}{2}(\boldsymbol{v} \bullet \boldsymbol{v})$$

with **v** being the horizontal velocity with respect to the ground, and ρ the density of the air (kg m^{-3}). Only horizontal velocity, not vertical velocity, is considered in the calculation because it is several orders of magnitude larger than the vertical component. Starting with the horizontal momentum equation

$$\frac{d\boldsymbol{v}}{dt} = -\frac{1}{\rho}\nabla P + F + f\boldsymbol{k}\ x\ \boldsymbol{v}$$

and taking the dot product of both sides, we obtain

$$\boldsymbol{v} \bullet \frac{d\boldsymbol{v}}{dt} = \frac{1}{\rho}(-\boldsymbol{v} \bullet \nabla P) + \boldsymbol{v} \bullet \boldsymbol{F} + 0$$

which can easily be simplified to the following equation using the aforementioned definition of KE:

$$\frac{dKE}{dt} = -\boldsymbol{v} \bullet \boldsymbol{\nabla} P + \boldsymbol{v} \bullet \boldsymbol{F} + KE\ \frac{dln\rho}{dt} \qquad (1)$$

where the first and second terms on the RHS represent generation and dissipation, respectively. This equation will from now on be referred to as Equation 1, which is used heavily in calculating the energetics of Earl. In addition, it is used to derive a kinetic energy budget equation in bulk form, following Dutton (1976). Given some function, f(x,y,z,t), we define a volume integral as follows:

$$F(t) = \int f(x, y, z, t)\ dV$$

Given that each point on the boundary has a velocity, **U**

$$\frac{\partial F}{\partial t} = \int \frac{\partial f}{\partial t} dV \; + \int f(s)(\boldsymbol{U} - \boldsymbol{V}) \bullet \boldsymbol{n} \, dS$$

The divergence theorem implies that

$$\frac{\partial F}{\partial t} = \int \frac{\partial f}{\partial t} dV + \int \nabla \bullet f \, (\boldsymbol{U} - \boldsymbol{V}) \, dV$$

so that

$$\frac{\partial}{\partial t}\left(\int KE \; dV \right) = \int \frac{\partial KE}{\partial t} dV \; + \int \nabla \bullet f \, (\boldsymbol{U} - \boldsymbol{V}) \, dV$$

which simplifies to

$$\frac{\partial}{\partial t} BKE = \; - \int \boldsymbol{v} \bullet \boldsymbol{\nabla} P \; dV - \int \boldsymbol{v} \; \bullet \; \boldsymbol{F} \, dV - \; \int \nabla \bullet KE(\boldsymbol{U} - \boldsymbol{V}) \qquad (2)$$

which will from now on be referred to as Equation 2.

Equations 1 and 2 are used in calculating the individual and bulk energetic quantities, respectively, as described in Chapter 3. In doing so, we define a rectangular control volume with a width of 400 km and z = 10 km, centered at the minimum surface pressure, following the movement of Earl at 20-min intervals during the 120-h integration of the innermost storm-following domain. First, individual energy quantities are analyzed. Then, the technical soundness of the budget process is verified, and finally, bulk energetic quantities are calculated.

Chapter 3. Results

3.1 Secondary Eyewall Formation

As mentioned in previous chapters, the simulation successfully captures the SEF of Earl, although it is slightly late in reproducing this cycle. Figure 5 shows the 1.5 km radar reflectivity within 110 km of the storm center at several times late in the simulation. Because the SEF does not begin until several days into the simulation, figures from earlier times are not shown. Early on 30 August, outer rainbands are contracting closer to the eyewall, but they have not yet formed concentric eyewalls. However, by later in the day and into 31 August, the rainband has formed into a fully concentric outer eyewall, creating a double eyewall structure similar to that shown in observations. It appears as if this outer eyewall weakens later on 31 August but then reappears. It finally dissipates on 01 September, as the inner eyewall also undergoes a partial collapse around the same time. We further investigate energetics of Earl at these times in order to understand how storm energy and intensity changes are associated with eyewall structural changes.

The azimuthally-averaged reflectivity and tangential winds, which provide a more axisymmetric view of the radial distribution of the storm, are shown in Figure 6. The RMW quickly decreases early during the simulation, situating itself approximately 25 km from the storm center by 29 August. It then remains relatively steady until 31 August, which also corresponds to the time of the peak of the secondary eyewall. As this double eyewall begins to dissipate, giving way to a newly formed single eyewall, the RMW slowly expands to around 35 km by the end of the model run. It is no coincidence that these two variables appear to be correlated, as reflectivity maxima often correspond to regions of strong

vertical motion in the atmosphere, which then translate to areas of strong tangential wind, especially near the surface.

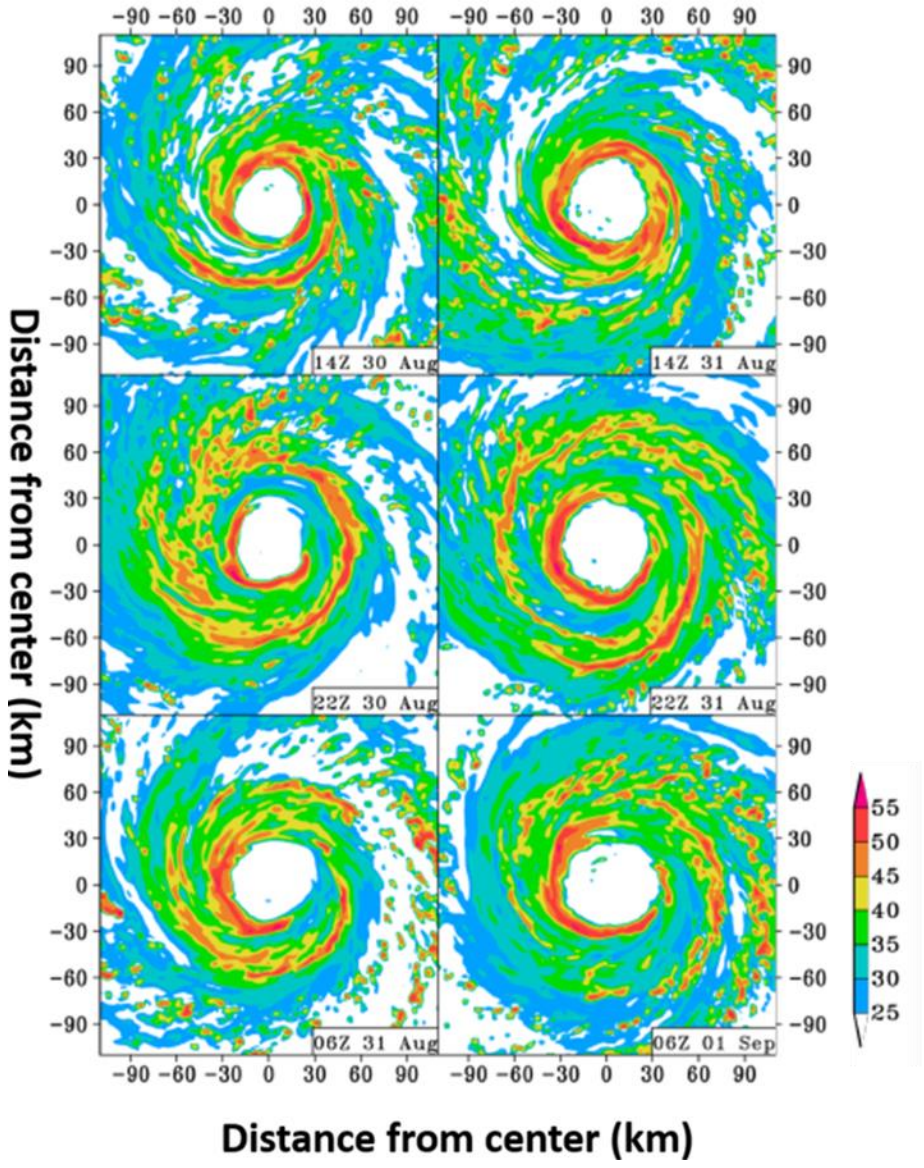

Figure 5: Simulated radar reflectivity (shaded, dBZ) at 1.5 km height at the times indicated in each panel; obtained from the innermost domain

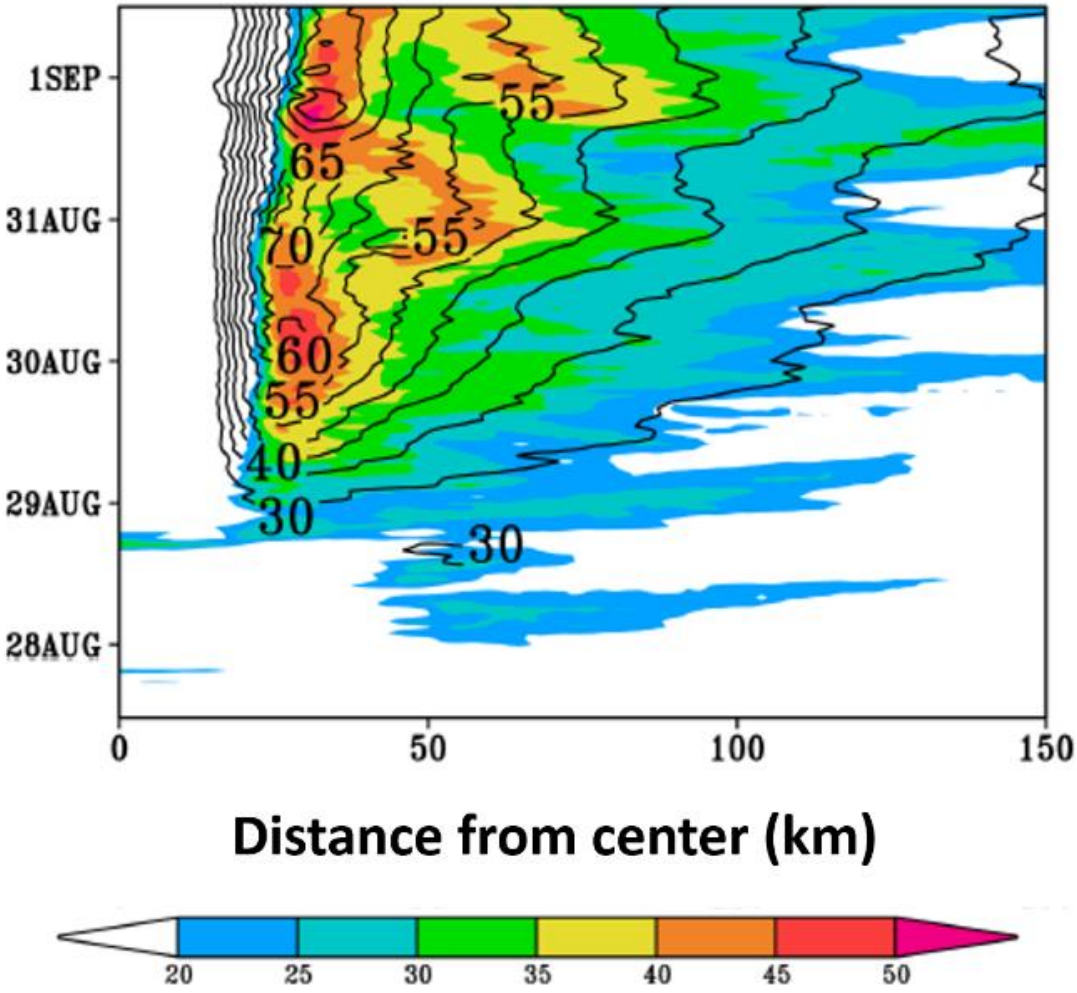

Figure 6: Azimuthally-averaged simulated radar reflectivity (shaded, dBZ) and tangential wind (contours, ms^{-1}); obtained from innermost domain

3.2 Energetics

3.2.1 Bulk Kinetic Energy

Before investigating the overall energy budget for Earl, the volume-averaged bulk kinetic energy (BKE) is analyzed in order to gain an understanding of the overall evolution of the system and its intensification. Before Earl undergoes RI, BKE is relatively constant at its initial value (Figure 7). However, by the time RI begins, the BKE is increasing steadily at a fast rate, doubling in just over 24 hrs. Around 31 August, when the outer

eyewall begins to form, BKE reaches a peak and then slowly declines for approximately 12 hrs. After then increasing again for nearly an entire day, the BKE reaches a second peak, this one greater in magnitude than the first, and slowly declines again after the outer eyewall reappears.

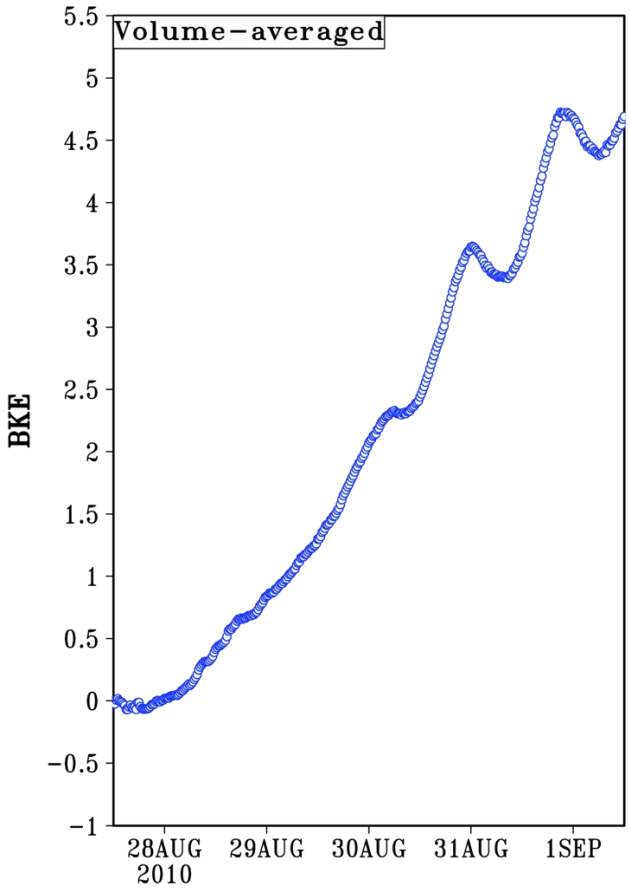

Figure 7: Volume-averaged bulk kinetic energy (BKE) normalized by the initial value of 2.88 x 10^8 J; for instance, a value of 2.5 corresponds to a value of BKE that is 250% of the BKE value at the initial time

Over the course of RI and the post-RI slow intensification, BKE increases by more than a factor of four. It is clear that RI, as well as the SEF, plays a major role in the energetic intensification of Earl, and that these two events are connected to other storm

variables such as tangential wind magnitude. The energetics of RI and SEF are therefore crucial to our understanding of and ability to forecast rapidly intensifying tropical cyclones. Additionally, it is evident that the BKE changes coincide fairly well with the intensity changes of Earl (Figures 3 and 7) with only minor differences, and therefore BKE is a useful indicator of hurricane intensity (Powell and Reinhold 2007; Hogsett and Zhang 2009).

3.2.2 Spatial Energetic Variability

Before analyzing the bulk energy budget through the use of Equation 2, an analysis of Equation 1 must be performed in order to verify that the budget is sound and that the data satisfies the governing physical laws. Because it is difficult to explicitly calculate the second term (dissipation) on the right-hand sides (RHS) of Equations 1 and 2 due to the presence of the friction variable, we instead calculate, using Equation 1, the RHS without the dissipation term, as well as the left-hand side (LHS), and take the difference between the two in order to find out in which locations of the storm the residual term is large and those where it is small. Figure 8 shows the residual term as a function of height and distance from the center of the storm. The residual is large in the boundary layer as well as the upper-level outflow region but is negligible elsewhere. This result is reasonable, as friction plays a large role in boundary layer processes, and because the upper-level outflow region is influenced by turbulent diffusion associated with the high velocity radial flow, which is especially true near the end of the intensification period when the outflow is strongest (at this time, Earl also contains multiple updrafts associated with the double eyewall). Additionally, these findings indicate that the budget is sound. As a result, we go on to perform the KE energy analysis.

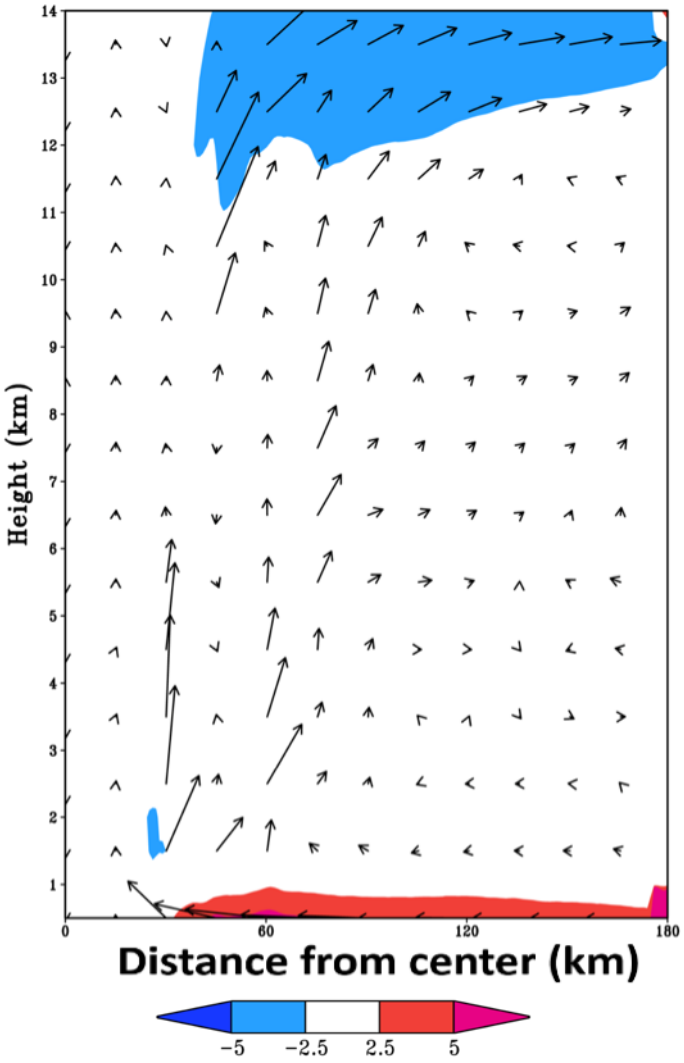

Figure 8: Budget residual (shaded, J m^{-3} s^{-1}) obtained from Equation 1 and used as a proxy for the frictional term

Because the cross-isobaric generation term is fairly dominant within the bulk energetic budget, it is important to understand the spatial and temporal variability of this term in a per-unit-volume sense using Equation 1. For this reason, Figure 9 shows the term at two different times, one near the beginning of the model RI and the other around the end of the post-RI slow intensification period. It is clear that during both times, cross-isobaric generation is maximized in the eastern quadrant of the cyclone, which is supported by

previous research that shows that this often occurs in the eastern and northeastern quadrants of other storms (Hogsett and Zhang 2009). However, we see an increase in areal coverage of negative generation late during RI, which helps, in addition to the SEF, to end the intensification process. Locations of cross-isobaric positive and negative generation are highly dependent upon the orientation of the storm-relative shear vector, which slightly varies from one storm to another, as well as temporally within each storm.

While the vertical extent of cross-isobaric positive generation remains nearly the same from the beginning to end of the intensification period, the negative component in the western quadrant increases substantially with height toward the end of the intensification. This is not true during early RI, however, when the eastern half is responsible for most of the positive generation up to about 7 km, while the majority of the western half negative component only reaches about 4 km. These results are in agreement with Hogsett and Zhang (2009), who found that the conversion of LE to KE is negative in the lowest 300 hPa and positive aloft during the early intensification stage because of the vertical distribution of radial flows and their spatial variability from the western to the eastern half. Additionally, our analysis shows that the KE maxima coincide spatially with the RMW, but, although the generation maxima are close to the RMW, the majority of cross-isobaric positive and negative generation occur just outside of the RMW, contrary to precipitation and many other atmospheric quantities which are often maximized inside the RMW (Wang 2002).

3.2.3 Bulk Kinetic Energy Budget

It is clear that the generation term varies spatially in both the horizontal and vertical, and that these structures change over time, especially with regards to RI and the SEF.

However, analyzing only the spatial structures is not enough to fully understand the evolution of the energetics of Earl. To do this, we perform a bulk energetic calculation

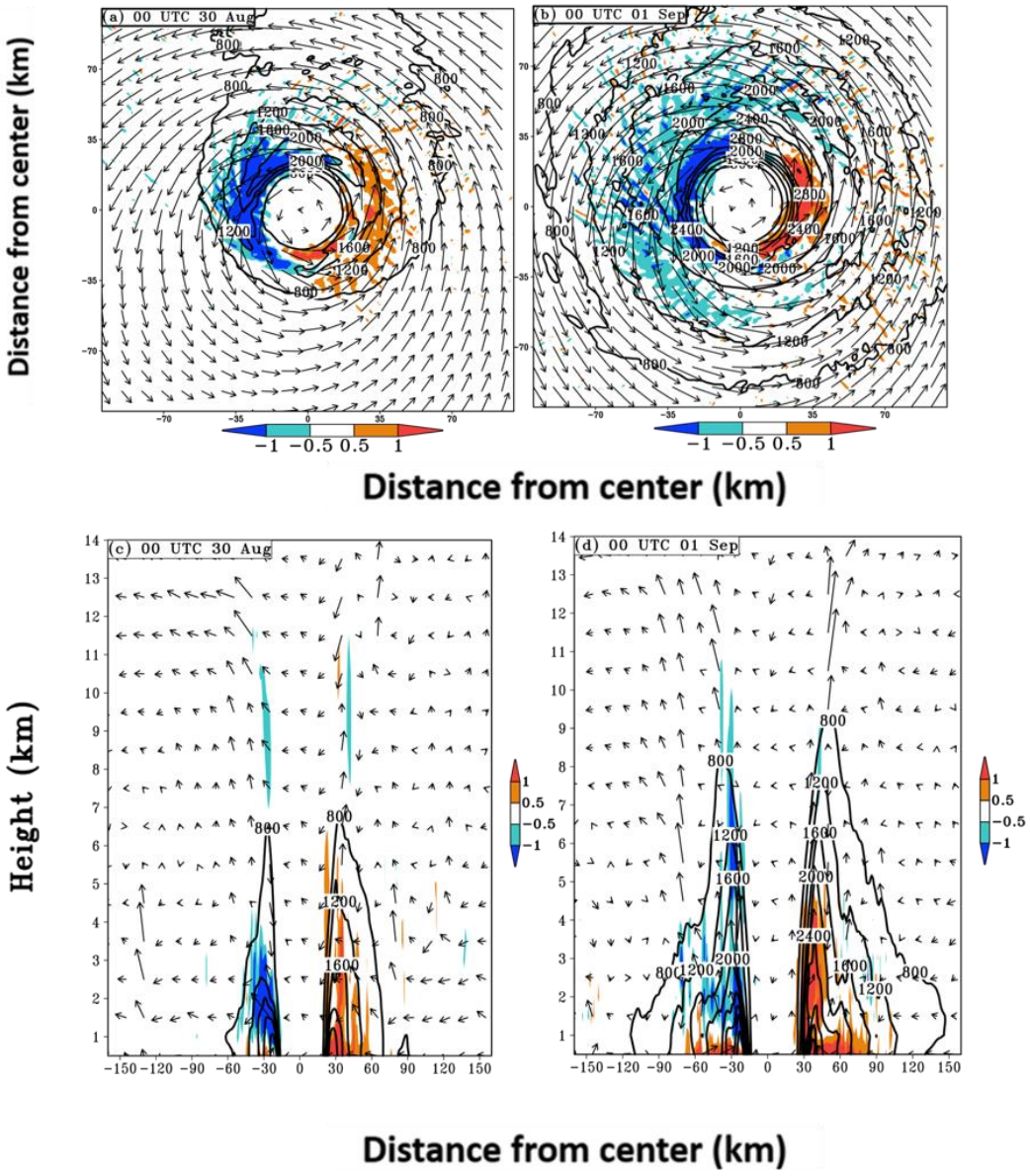

Figure 9: Generation term (shaded, J m^{-3} s^{-1}) from Equation 1, kinetic energy (contours, J m^{-3}), and wind vectors; top two panels are horizontal cross-sections at the 1.5 km level, while bottom two panels are east-west vertical cross-sections

through the use of Equation 2, which provides an integrated form of Equation 1. In performing a bulk calculation, it is important to choose a calculation domain size wisely, as the terms are sensitive to such domain size.

Figure 10 shows the evolution of the bulk energy budget terms over the course of the 120-h simulation of the innermost domain, calculated over a rectangular control volume with a width of 400 km and a maximum height of 10 km. KGEN is relatively small until RI begins, when it starts to rapidly increase. Later during and after RI, however, several fluctuations occur in association with the double eyewall formation and collapse. The residual (dissipation) undergoes similar changes throughout RI, mainly decreasing while undergoing fluctuations associated with the double eyewall cycle, although these fluctuations are smaller in magnitude than those of KGEN. The evidence of the SEF is also contained in the KTEN term, which remains positive and relatively steady until the SEF cycle begins.

A more detailed view of the KGEN term, through its positive and negative volume-averaged components, is shown in Figure 11. Initially, before RI begins, the positive and negative terms increase at similar rates. However, as the model RI starts, the two start to diverge. This difference increases substantially as RI continues, with the largest difference occurring near the end of the intensification period. The SEF is evident in both the positive and negative KGEN terms, which is expected, since both terms depend heavily on the wind field. It is interesting to note that the terms appear to begin to converge again after the intensification, but the simulation would need to be extended to further investigate this feature.

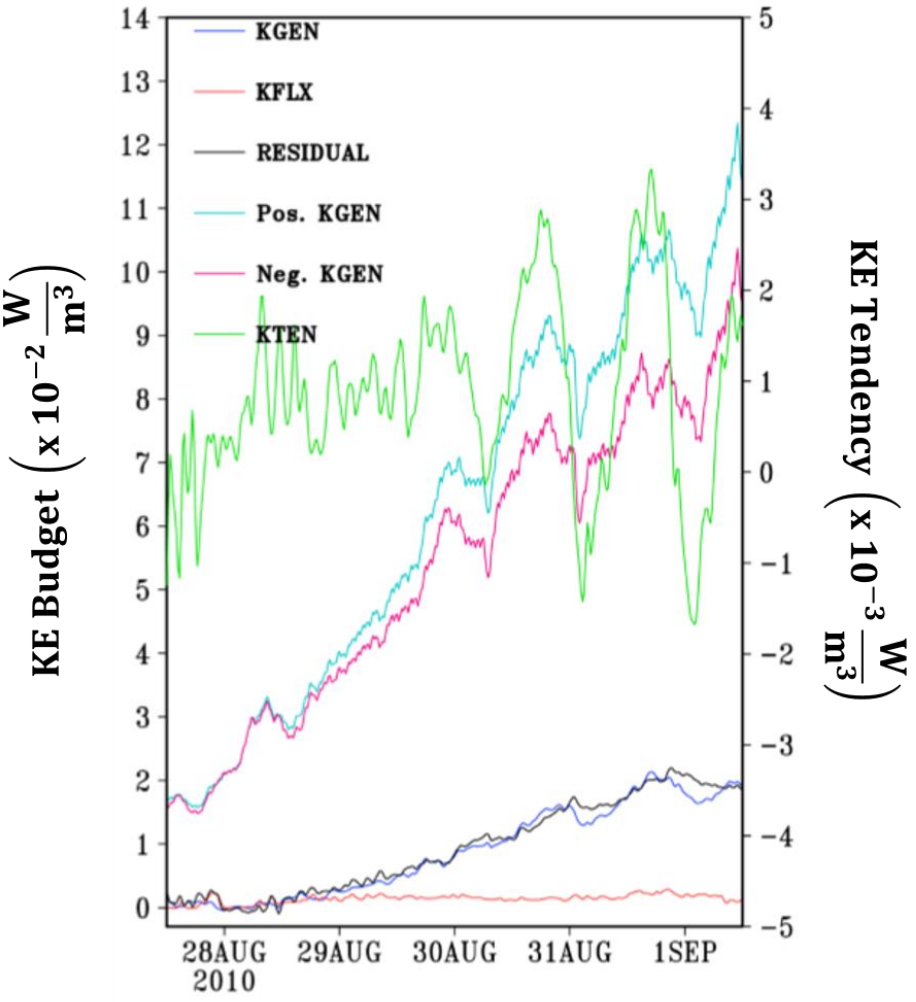

Figure 10: Time series of the volume-averaged BKE budget obtained through the use of Equation 2, including cross-isobaric generation (KGEN, blue) and its positive (Pos. KGEN, cyan) and negative (Neg. KGEN, magenta) components, boundary flux (KFLX, red), BKE tendency (KTEN, green), and the residual (RESIDUAL, black; used as a proxy for friction term)

3.2.4 Sensitivity to Domain Size

The bulk energetic quantities provide a decent sense of the overall, domain-integrated, volume-averaged quantities of cross-isobaric generation, storm total kinetic energy tendency, boundary flux, and the friction residual term. However, because these

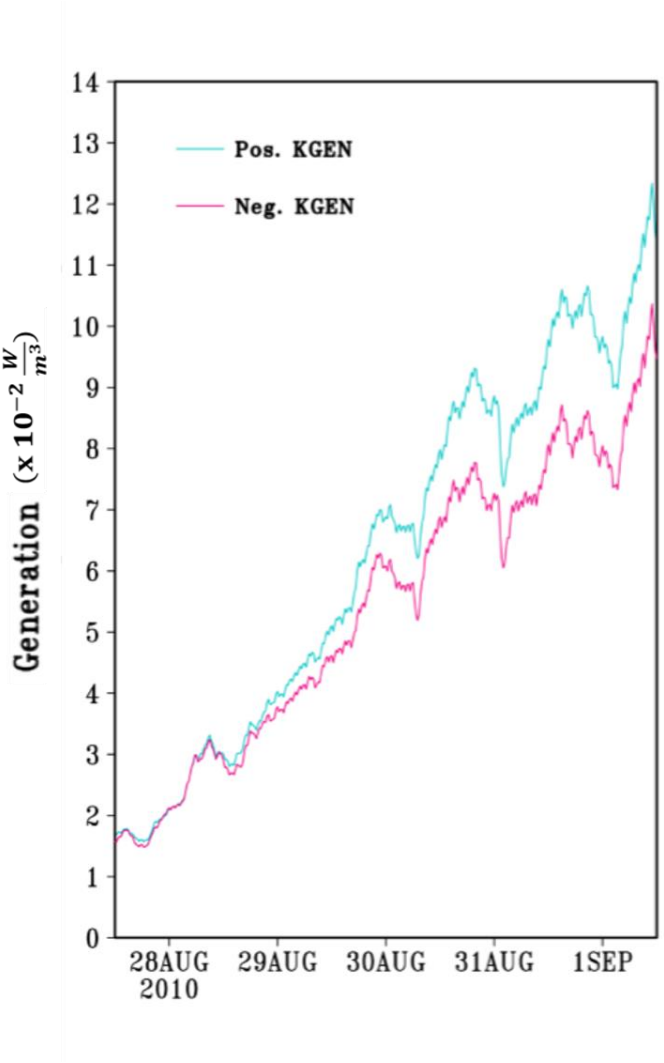

Figure 11: Positive and negative components of the volume-averaged KGEN

quantities are averaged over a domain, this control volume domain cannot be chosen arbitrarily. We therefore perform a sensitivity experiment to justify the use of our chosen

control volume. In this experiment, domain width is varied from 400 km to 200 km to 100 km. In all cases, the minimum height is 0.1 km, the maximum height is 10 km, and the atmospheric levels in between are included at intervals of 0.5 km.

In general, as domain width is decreased, the evidence of the SEF slowly erodes, especially within the KTEN term (Figure 12). The magnitude of the fluctuations associated with the formation and collapse of the double eyewall structure is much smaller in the 200 km than the 400 km case, and such fluctuations are virtually nonexistent when using the 100 km control volume. This is likely due to the fact that the 200 and 100 km volumes are too small and do not fully contain the outer eyewalls, and therefore do not successfully capture the changes in KTEN associated with the SEF. As shown in Figure 9, kinetic energy is generally maximized near the RMW and the eyewalls. Therefore, 200 km and 100 km exclude some of these kinetic energy maxima.

The SEF is also evident in the KGEN term, mainly within the 400 km and 200 km experiments. However, the 100 km lacks such evidence. It is interesting to find that the KGEN fluctuations associated with the SEF are found in KGEN but not KTEN in the 200 km domain; this is likely explained by the fact that the KGEN depends more heavily on the overall wind field than does KTEN, and, although the 200 km domain excludes the kinetic energy maxima associated with the outer eyewall, it contains some of the cross-isobaric generation associated with the outer eyewall wind field. This hypothesis is further supported by the fact that the 200 km domain contains large increases in KGEN during RI, but such increases become smaller in magnitude (relative to the pre-RI value) within the 100 km calculation.

In addition, the magnitude of the KFLX term relative to the other terms varies with domain size. More specifically, it increases with decreasing domain size, which is understandable because, with the smaller domain sizes, more energetic changes are occurring at the boundary, such as those occurring in association with the inner and outer eyewalls.

Finally, the overall magnitude of the terms, especially of the KGEN and residual terms, decreases as domain size increases. This is a result of the fact that the small domain sizes do not contain large "quiet regions" of inactivity, such as outside the outer eyewall. As a result, the volume-averaged quantities within the smaller domain are larger than those within the larger domains, while on the other hand, non-volume averaged quantities would exhibit an increase with increasing domain size.

Through this sensitivity experiment, it can be concluded that a 400 km domain, with a maximum height of 10 km, successfully captures the energetic features associated with the RI and SEF, as well as the storm generation within the Planetary Boundary Layer (PBL). A larger domain would include unnecessary regions of inactivity, while smaller domains do not contain important structural features. A sensitivity experiment in which the maximum height is varied was also performed, although these results (not shown) were similar to those of the 10 km height experiment.

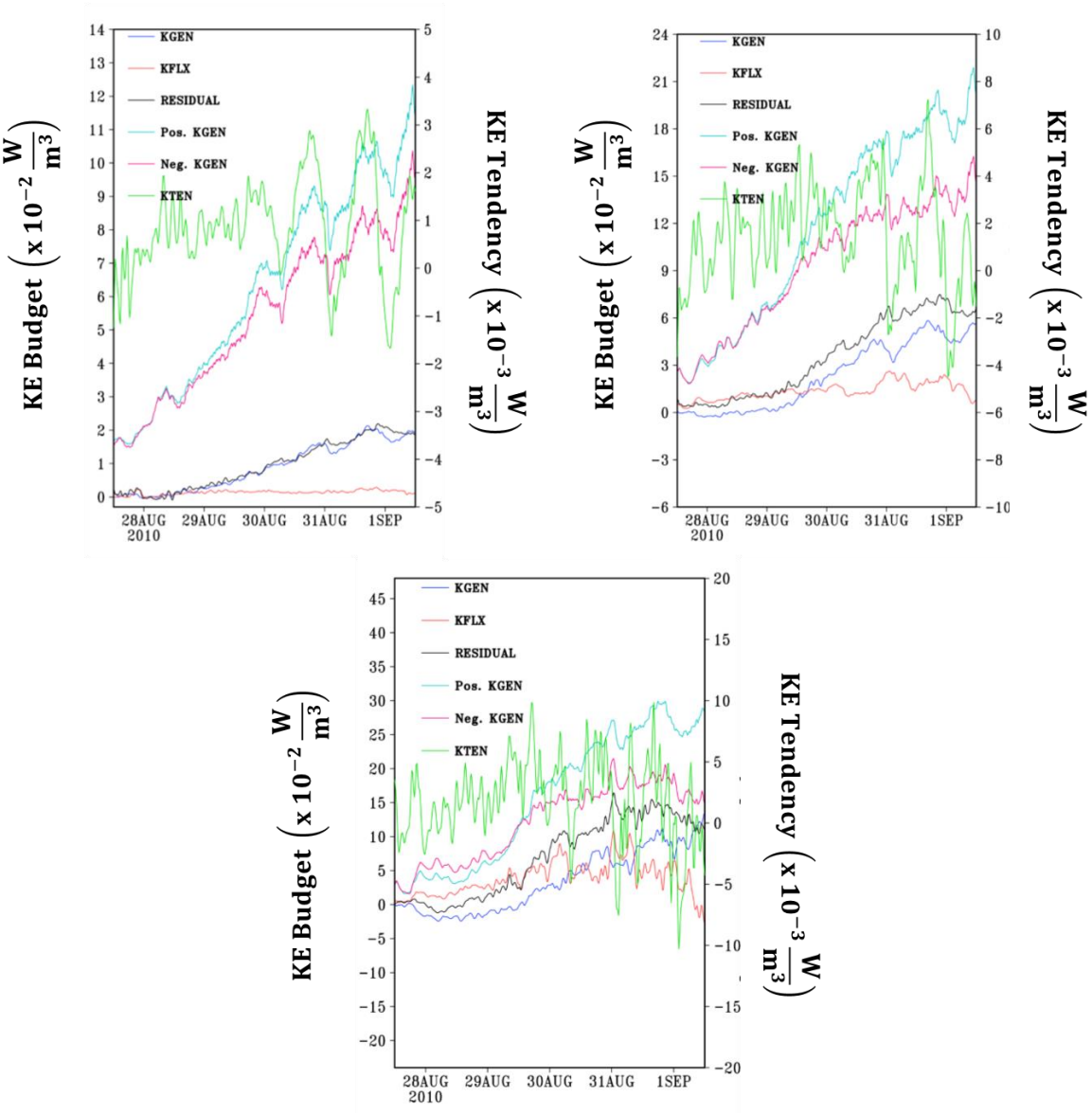

Figure 12: Time series of the volume-averaged budget terms for domain widths of 400 km (top left), 200 km (top right), and 100 km (bottom); all figures are for a maximum domain height of 10 km

Chapter 4. Summary and Conclusions

In this study, several aspects of Hurricane Earl (2010) have been analyzed, including the intensity changes, SEF, and storm structure, along with the ability of the model to reproduce such features. Additionally, the energetic changes before, during, and after RI are investigated through the analysis of the time evolution of bulk energetic quantities. The spatial variability of these quantities is also analyzed in order to better understand where KE and its generation are maximized, as well as the locations where the budget residual is largest, indicating that these are the regions where frictional dissipation is most prominent.

The simulated storm track, intensity, and structure compare reasonably well to observations, and the simulation successfully reproduces the SEF, albeit a few hours later than it occurs in the observations. As a result, the end of the intensification period also occurs later in the simulation. The SEF and formation of an outer eyewall help to end RI by decreasing the flux of moisture and heat to the center of the storm, thereby slowing down and eventually stopping the intensification process. It is also shown that the evolution of BKE compares reasonably well to the intensity changes of Earl, and that the evidence of the SEF is contained within the BKE. A further analysis of the KE budget shows that the residual term is largest within the boundary layer and upper-level outflow regions, indicating the likelihood of frictional dissipation occurring the boundary layer and turbulent diffusion occurring in the upper-level outflow layer. Elsewhere, the residual term is smaller and negligible, indicating that the dissipation term is small in these regions, and that the budget is mathematically sound.

The cross-isobaric positive and negative generation terms evolve in a similar fashion until RI begins, at which time they diverge; large differences between positive and negative generation provide a useful indication of a rapidly intensifying cyclone. Generation is maximized in the eastern portion of the storm and minimized in the western portion, both occurring near the location of the inner eyewall. The volume-averaged BKE increases substantially during RI but slows during the SEF. KTEN is mainly positive during intensification with the exception of fluctuations occurring during the SEF, although such fluctuations become less evident as the domain size over which the calculation is performed is decreased. As domain size decreases, KFLX becomes larger in magnitude relative to the other terms, as more processes are occurring near the boundary of the domain.

Although only Earl has been investigated for the purposes of this study, the findings can be widely applied to other storms undergoing RI. In general, RI can last for several days, but after substantial intensification has occurred, SEF eventually begins and slows the intensification process. Cross-isobaric KE generation accounts for much of the energy increase during RI and can therefore be used as a reasonable indicator, along with BKE, of intensification. For this reason, future work should further investigate positive and negative KGEN, as well as BKE, and provide methods for which they can be calculated within models in real time.

References

Braun, S. A., 2002: A cloud-resolving simulation of Hurricane Bob (1991): Storm structure and eyewall buoyancy. *Mon. Wea. Rev.,* **130**, 1573–1592.

Chen, H., and S.G. Gopalakrishnan, 2015: A Study on the Asymmetric Rapid Intensification of Hurricane Earl (2010) Using the HWRF System. *J. Atmos. Sci.*, **72**, 531-550.

Davis, C. A., and Coauthors, 2008: Prediction of Landfalling Hurricanes with the Advanced Hurricane WRF Model. *Mon. Wea. Rev.*, **136**, 1990–2005.

DeMaria,M., M.Mainelli, L. K. Shay, J. A. Knaff, and J. Kaplan, 2005: Further Improvements to the Statistical Hurricane Intensity Prediction Scheme (SHIPS). *Wea. Forecasting*, **20**, 531–543.

Donelan, M. A., B. K. Haus, N. Reul, W. J. Plant, M. Stiassnie, H. C. Graber, O. B. Brown, and E. S. Saltzman, 2004: On the limiting aerodynamic roughness of the ocean in very strong winds. *Geophys. Res. Lett.*, **31**.

Dutton, J.A., 1976: *The Ceaseless Wind*. McGraw-Hill, 576 pp.

Frank, W. M., 1977: The structure and energetics of the tropical cyclone II. Dynamics and energetics. *Mon. Wea. Rev*., **105**, 1136–1150.

Hogsett, W., and D.L. Zhang, 2009: Numerical Simulation of Hurricane Bonnie (1998). Part III: Energetics. *J. Atmos. Sci.* **66**, 2678-2696.

Hong., S.Y., Noh, Y., and Dudhia, J., 2005: A New Vertical Diffusion Package with an Explicit Treatment of Entrainment Processes. *Mon. Wea. Rev.*, **134**, 2318-2341.

Kain, J.S.: The Kain-Fritsch Convective Parameterization: An Update. *J. Appl. Meteorol.*, **43**, 170-181.

Kaplan, J., and M. DeMaria, 2003: Large-scale characteristics of rapidly intensifying tropical cyclones in the north Atlantic basin. *Wea. Forecasting,* **18,** 1093–1108.

McBride, J. L., 1981: Observational analysis of tropical cyclone formation. Part III: Budget analysis. *J. Atmos. Sci.*, **38**, 1152–1166.

Powell, M.D., and T.A. Reinhold, 2007: Tropical Cyclone Destructive Potential by Integrated Kinetic Energy. *Bull. Amer. Meteor. Soc.* **88**, 513-526.

Rogers, R., and Coauthors, 2006: The Intensity Forecasting Experiment: A NOAA multiyear field program for improving tropical cyclone intensity forecasts. *Bull. Amer. Meteor. Soc.*, **87**, 1523–1537.

Rogers, R.F., P.D. Reasor, and J.A. Zhang, 2015: Multiscale Structure and Evolution of Hurricane Earl (2010) during Rapid Intensification. *Mon. Wea. Rev.*, **143**, 536–562.

Stevenson, S.N., K.L. Corbosiero, and J. Molinari, 2014: Convective Evolution and Rapid Intensification of Hurricane Earl (2010). *Mon. Wea. Rev.*, **142**, 4364-4380.

Susca-Lopata, G., J. Zawislak, E.J. Zipser, and R.F. Rogers, 2015: The role of observed environmental conditions and precipitation evolution in the rapid intensification of Hurricane Earl (2010). *Mon. Wea. Rev.*. **143**, 2207-2223.

Tuleya, R. E., and Y. Kurihara, 1975: The energy and angular momentum budgets of a three-dimensional tropical cyclone model. *J. Atmos. Sci.*, **32**, 287–301.

Wang, Y., 2002: Vortex Rossby waves in a numerically simulated tropical cyclone. Part I: Overall structure, potential vorticity, and kinetic energy budgets. *J. Atmos. Sci*., **59**, 1213– 1238.

Zhu, T., D.-L. Zhang, and F. Weng, 2004: Numerical simulation of Hurricane Bonnie (1998). Part I: Eyewall evolution and intensity changes. *Mon. Wea. Rev.*, **132**, 225–241.